**Islamic Azad University
Mashhad Branch**

Experimental, Franc2d, and DDM simulation to determine the anisotropic tensile strength of brittle material

Vahab Sarfarazi[*1], Hadi Haeri[2]

1. Department of Mining Engineering, Hamedan University of Technology, Hamedan, Iran
2. Department of Mining Engineering, Bafgh Branch, Islamic Azad University, Bafgh, Iran

Abstract

In this paper, a compression-to-tensile load converter device is developed to determine the anisotropic tensile strength of brittle material. A cubic sample with an internal pore was used as the test specimen, and a series of finite element analysis and DDM simulations were performed thereafter to analyse the effect of pore dimensions on the stress concentration, as well as to render a suitable criterion for determining the anisotropic tensile strength of concrete. The results obtained by this device show that the tensile strength of concrete is similar in different directions because of the homogeneity of bonding between the materials.

Keywords: compression to tensile load, anisotropic tensile strength of concrete.

1. Introduction

The tensile strength of brittle material such as concrete and rock is a crucial design parameter for building structures like concrete dams, airfield runways, concrete roads and pavements, and others. Therefore, many experimental and theoretical studies have been carried out to determine the tensile strength of concrete (Zhou 1988; De Larrard and Malier 1992; Gomez et al. 2001; Zheng et al. 2001; Calixto 2002; Zain et al. 2002; Swaddiwudhipong et al. 2003; Mobasher et al. 2014; Gerges et al. 2015; Ibrahim et al. 2015; Liu et al. 2015; Silva et al. 2015). The tensile strength obtained from the uniaxial tensile test is more reliable than other methods; however, this test requires far more care as compared to indirect methods. Especially after the production of strong epoxy-based adhesives, uniaxial tensile tests have thrown up a few problems. Many previous experimental studies for determining uniaxial tensile strength have failed because of unexpected crushing due to local stress concentrations. Another difficulty in uniaxial tensile tests is that the test specimen is often under the influence of momentary effects, during the test, due to eccentricity. The tensile strength of concrete will be different in various directions due to the non-homogeneity of bonding between concrete materials. Furthermore, the accumulation of weak plane in the special direction also leads to the anisotropy of concrete's tensile strength. The objective of this paper is to develop a new loading device called the compression-to-tension converter (CTT), which can apply tensile stress on the concrete specimen from different directions.

----
*Corresponding author.
E-mail address (es): vahab.sarfarazi@gmail.com

The proposed device will be designed such that it can be used alongside most commercially available compression loading machines. It should ideally be durable, inexpensive, and easy to use. The concept is to apply compressive loads to the top and bottom of the pore, so that the specimen is subjected to uniaxial tensile stress.

2. Compression-to-tension load converter device

The objective of a compression-to-tension load converter device (CTT) is to determine tensile strength for specimens containing internal pores, under uniaxial tension. Its primary design requirement is to allow alternating applications of tensile and compressive load on the same specimen, placed in a conventional compression machine. The compression-to-tension load converter device comprises several parts. The first part, which has a 'U' shape, is built from stainless steel. This part is divided to two separate segments, i.e. 'L'- and 'l'-shaped segments. The second part with a 'Π' shape is undividable.

The third part comprises two stainless steel semi-cylindrical shapes, with dimensions of 60×10×60mm. The fourth part is composed of two blades with the dimensions of 20×10×190mm. The setup procedure of the CTT device consists of six stages. Firstly, the third part is inserted into the pore. Secondly, the L-shaped segment of the first part is placed in the left side of the specimen. Thirdly, the first blade of the fourth part is placed through the pore such that its upper surface is in contact with the cylindrical steel, i.e. from part 3, and its lower surface is in contact with the L-shaped segment. Fourthly, the second part is placed at the right

side of the specimen. In the fifth stage, the second blade of part 4 goes through the pore such that its lower surface is in contact with the cylindrical steel of part 3, and its upper surface is in contact with the Π-shaped segment of part 2. In the sixth stage, the l-shaped segment is screwed to the L-shaped segment of part 1, thereby completing the apparatus setup. Therefore, the upper cast is in contact with the lower cylindrical steel and the lower cast is in contact with the upper cylindrical steel. When this setup is placed between the uniaxial loading frames, the upper loading frame compresses the upper cast, such that the lower part of the pore is compressed. Similarly, the lower loading frame compresses the lower cast such that the upper part of the pore is compressed. The compression of the upper and lower parts of the pore brings the specimen to tensile loading (Figs. 1, 2 and 3).
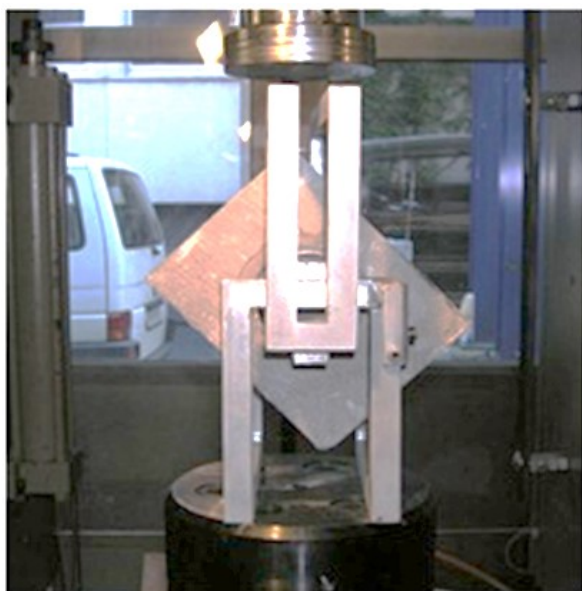

Fig. 1 The set up procedure of CTT device

By rotating the specimen inside the CTT device, tensile load is applied to the sample from different directions. Three different configurations were investigated: 1) the vertical side of the sample is parallel to the loading axis, 2) the vertical side of the sample returns 45° non-counter clockwise to the loading direction, and 3) the vertical side of the sample returns 45° counter clockwise to tensile load direction.

3. Experimental and numerical studies
The objective of laboratory testing is to determine the anisotropic tensile strength of the concrete specimen and to assess the performance of the CTT device. Numerical simulation is performed for better understanding of stress distribution in the model.
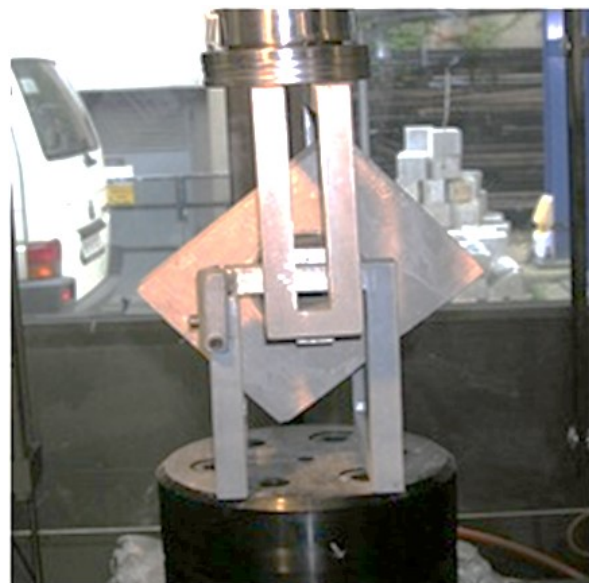

Fig. 2 The set up procedure of CTT device

The discussions in this chapter are divided into four sections. The first section describes the technique of preparing the specimens, while the second section is focused on the testing procedure for loading the specimens as well as general experimental observations. The third section describes the procedure of numerical simulation, and the fourth section discusses the experimental and numerical results.
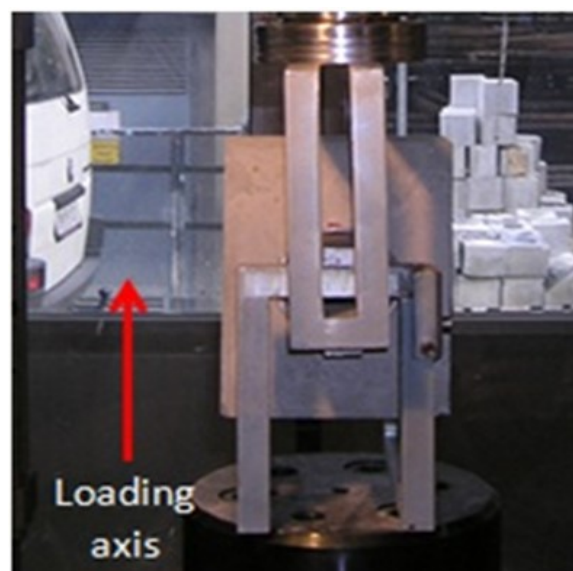

Fig. 3 The set up procedure of CTT device

3.1 Preparation of the internally pored specimens
The material mixture is prepared by combining water, fine sand, and Ordinary Portland Cement in a blender. Crushed limestone sand with 2.57g/cm^3 of specific

gravity and 2.75cm^2/g of fineness were used in a fine aggregate.

The mixture is then poured into a fibreglass cast with internal dimensions of 15×19×6cm. The cast consists of two discrete cubes bolted together. The fresh mixture is vibrated and then stored at room temperature for eight hours, till the specimens unmold. Then, a core with a diameter of 7.5cm and height of 60cm is removed from the centre of the samples via dry drilling, such that the ratio of pore diameter (7.5cm) to sample width (15cm) is 0.5. Based on the configurations described above, three similar samples were prepared and tested under direct tensile load.

3.2 Tensile strength test procedure
Figure 4 shows the test arrangement for direct tensile strength testing. The CTT device with the specimen is installed in a compression load frame. A 30-ton hydraulic load cell applies compressive load on the CTT end plates. An electronic load cell is used to measure the increase in applied load. To isolate the effect of the loading rate from the results, a constant load of 0.02 MPa/s was applied on all specimens. This rate is within the range recommended by BS1881-117 (1983) for tensile splitting strength testing. Three specimens are tested under direct tensile loading. A tensile failure is induced at or near the mid-section of all specimens, within 2–3 minutes (Fig. 4 a-c).

For calculation of far-field tensile stress in the direct tensile test, the far-field failure load is divided into a surface area of blades measuring 2×6 cm. However, according to the Cersh theory, far-field tensile stress is distributed non-uniformly around the circle and, therefore, it cannot be a proper representative for the tensile strength of concrete material. Numerical simulation is necessary to determine the relationship between far-field tensile stress, the ratio of pore diameter to sample width, and the stress concentration at corners of the pore. The output of the numerical simulation can be used to determine the real tensile strength of concrete.
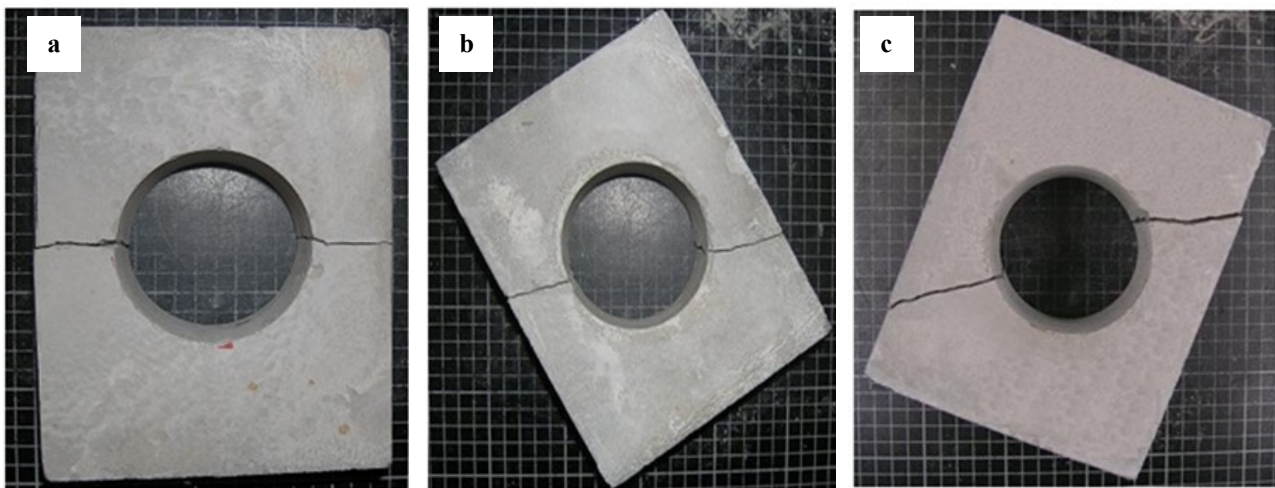

Fig. 4 Failure pattern in a) vertical sample, b) non counterclockwise oriented sample and c) counterclockwise oriented sample.

3.3 Finite Element Simulation
A two-dimensional finite element code, FRANC2D/L (FRacture ANalysis Code for 2-D Layered structures), was used to simulate the effect of pore dimension on stress concentration around the pore. This code was originally developed at Cornell University and modified for multi-layers at Kansas State University. It is based on the theory of linear and nonlinear elastic fracture mechanics (Wawrzynek and Ingraffea 1987). The general methodology starts from the pre-processing stage, where the geometry, mesh, material properties, and boundary conditions are specified. In the post-processing stage, loading conditions, crack definition, and crack growth process are specified. Figure 5 shows the finite mesh with boundary and loading conditions. The upper and downward sides of the model are fixed in 'x' direction, while the left and right sides are fixed in 'y' direction. To obtain a detailed distribution of the induced stress, up to 400 elements have been used in the models. Four samples were prepared with different ratios of pore diameter (D) to sample width (B); i.e. D/B= 0.125, 0.25, 0.375, and 0.5, respectively (Fig 5). These models were subjected to internal tensile stress of 10 MPa. The analyses are made assuming that concrete is linearly elastic and isotropic. The elastic modulus and Poisson's ratio of the model are assumed to be 25 GPa and 0.20.

The objective of the model analysis is to determine that there is no compressive stress at the middle of the specimen. The specimen can fail under tensile loading even before failure by shear stress occurs at both ends of the specimen. Failure under tensile loading occurs at the mid-length of the specimen.
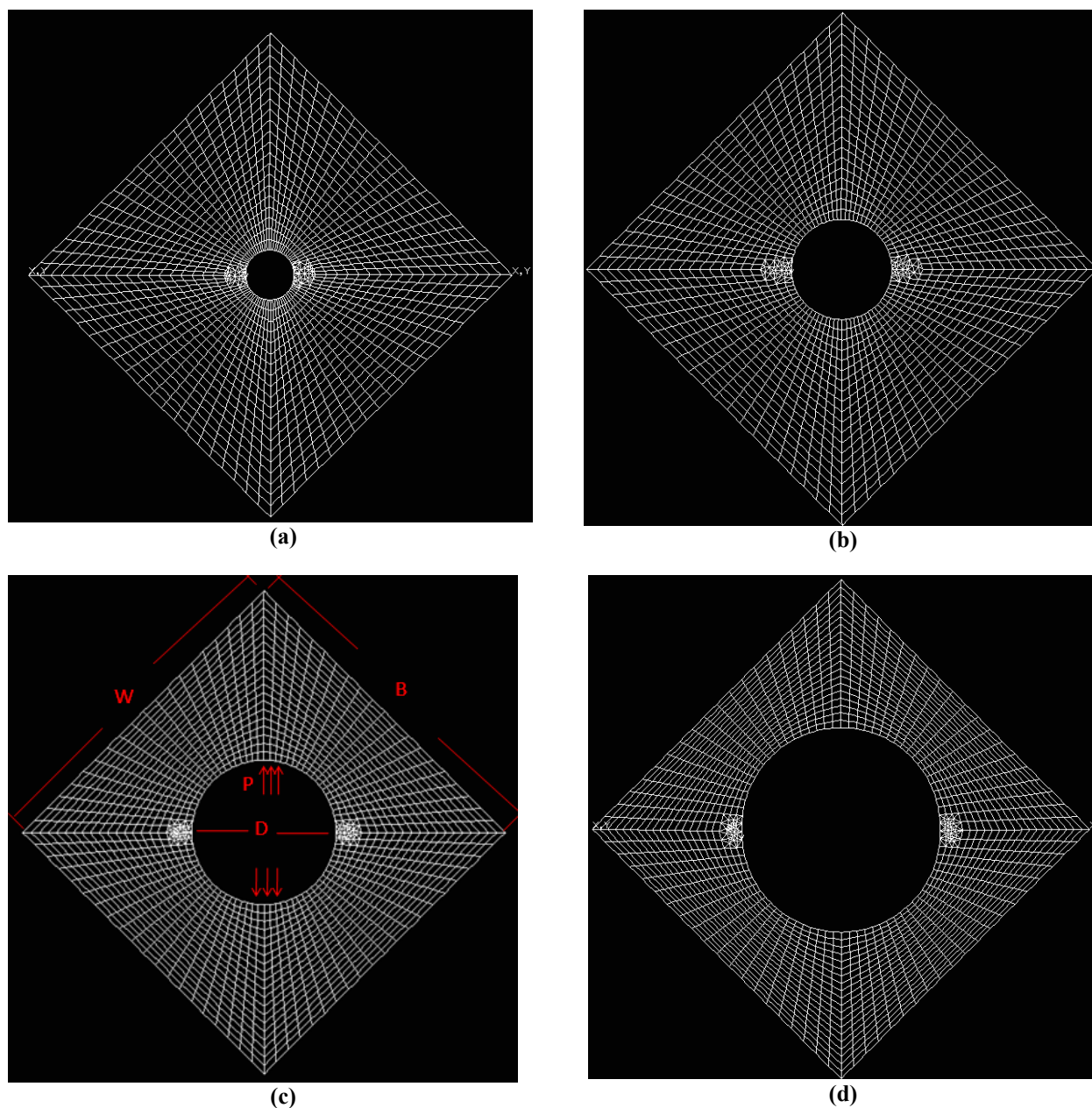
(a)

(b)

(c)

(d)

Fig 5 shows finite mesh with boundary and loading conditions

Figure 6 shows tensile stress distribution in the samples for different ratios of pore diameter to sample width. The model shows concentrated tensile stress at the left and right corners of the pore. The compressive stress is also concentrated at the top and bottom of the pore. Since the tensile strength of material is less than its compressive strength, these models experience failure at the corner of specimen, prior to failure under compression load at the vertical-section.

The maximum shear and tensile stress occur near the applied load areas. In addition, the value of tensile stress at the corner of the circle is more than the shear stress in all samples, whereas the tensile strength of the material is less than its shear strength. Therefore, these

models experience tensile failure at the corner of specimen, before failure under shear load at the centreline.

From the results of the numerical analysis, it can be concluded that the model with the internal bore is suitable for use with the compression-to-tension load converter (CTT). Since distribution of tensile stress in the model is more than the far-field tensile stress, the latter therefore could not directly be considered a measure of the tensile strength of concrete material. For determination of the real tensile strength, the relationship between concentrated tensile stress, far-field tensile stress, and pore diameter should be specified.
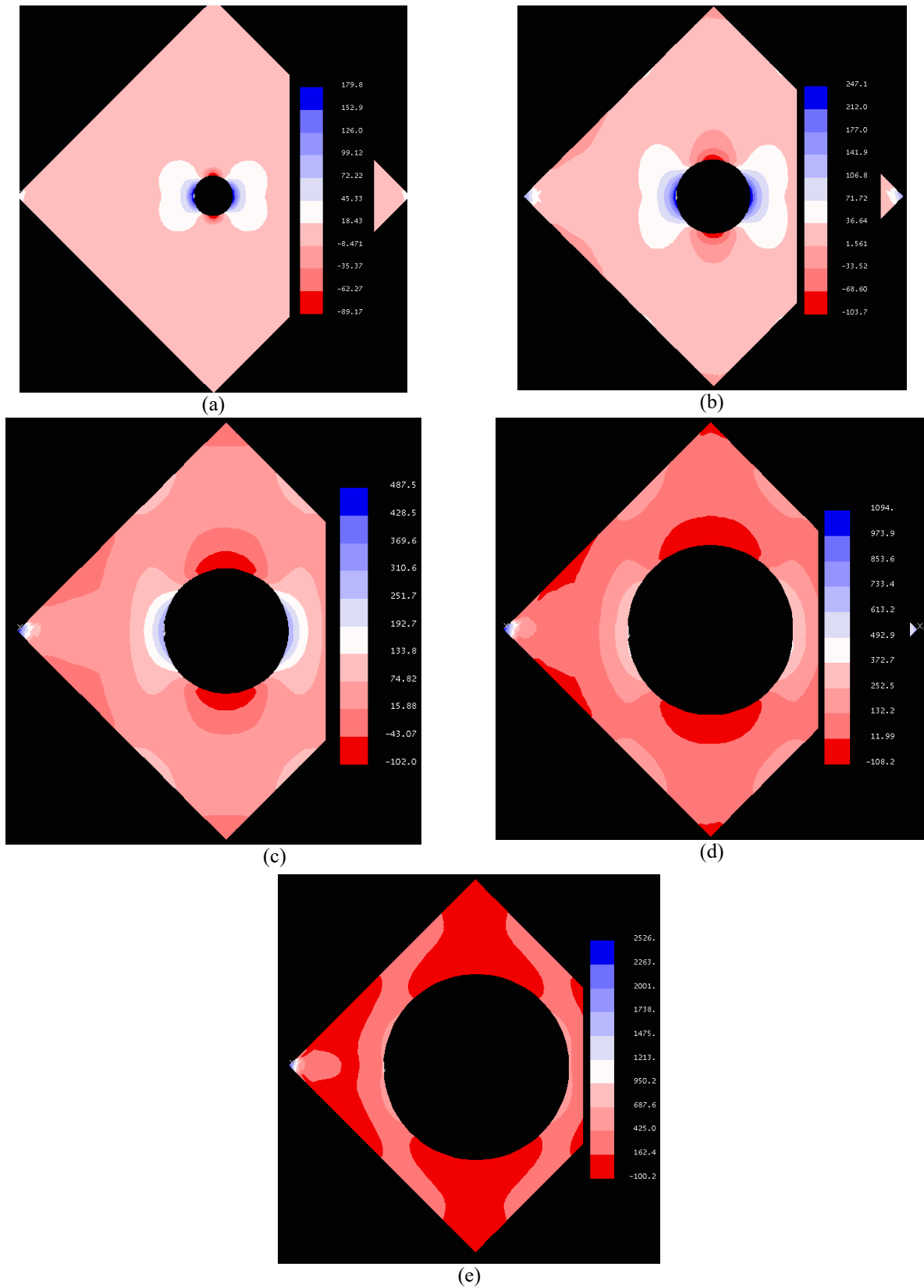
Fig. 6 the stress distribution in model with different hole diameter of, a) 0.125, b) 0.25, c) 0.375 d) 0.5.

Figure 7 shows the crack growth in numerical models. As can be seen, two tensile cracks start from both sides of the hole and propagate horizontally, till restricted in middle of the model.

Figure 8 shows the variation of normalized tensile stress concentrations at the corners of the pore as per the different ratios of circle diameter to sample width. From the curve on these data, it's possible to calculate the normalized tensile stress at the pore boundary (S2/Pt) as follows:

$$S2/Pt=3(D/B) +1 \qquad (1)$$

This equation shows that when far-field tensile load (Pt) is applied to the intact sample (D=0.0), the tensile stress distribution in the model, S2, is equal to Pt. This means that the tensile load is distributed uniformly in the model in the absence of the pore, which is logically acceptable. From another point of view, this equation shows that when the model is loaded under far-field tensile stress, the tensile stress concentration at the pore corners can be calculated using Eq. 1. For example, when far-field failure stress of 1.24 MPa is applied in the CTT physical test with D/B=0.5, the tensile stress concentration at the pore corners (S2) is 3.1 MPa, according to Eq. 1. When S2 reaches 3.1 MPa, it can overcome to the tensile strength of the material. Therefore, the ultimate tensile stress at the circle corners (S2) is registered as the real tensile strength. Based on this finding, Table 1 shows the comparison of tensile strength of concrete in three different directions.
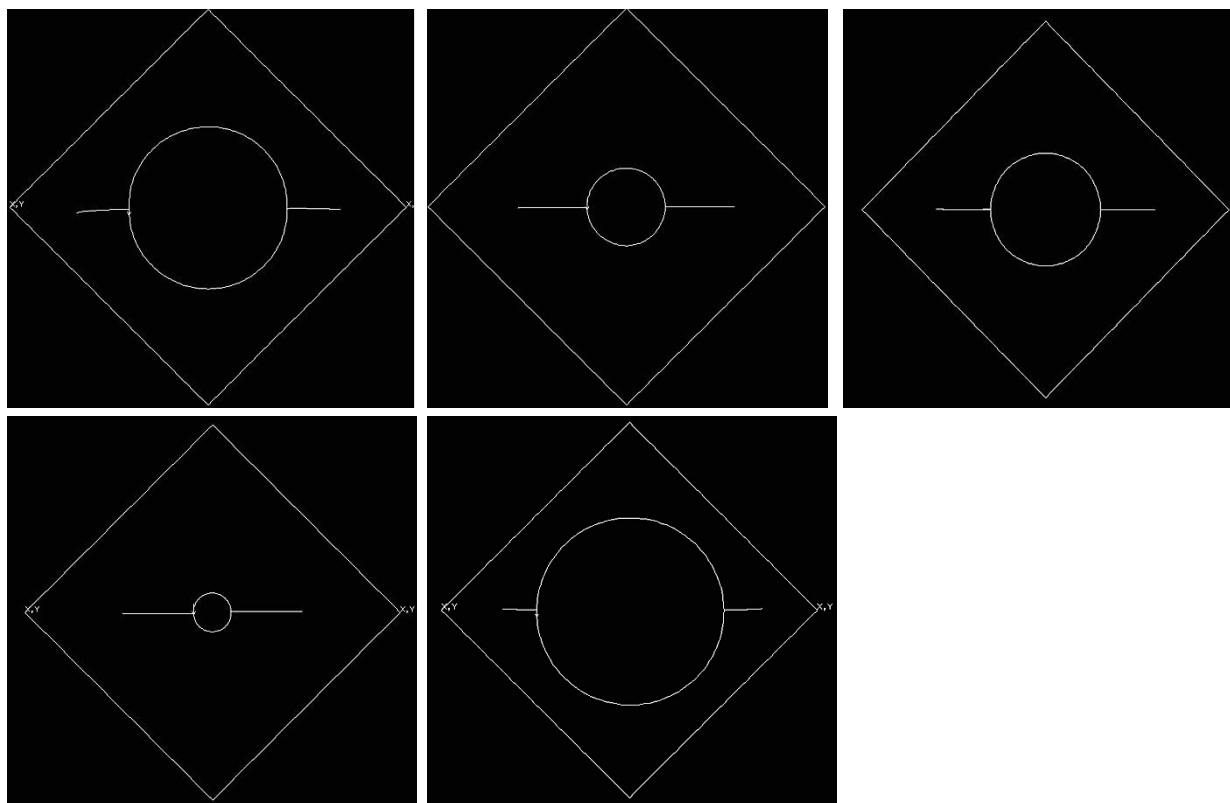

Fig 7 crack growth in numerical models with hole diameter of, a) 5 mm, b) 10 mm, c) 15 mm and d) 20 mm.

3.4 Comparison of the strength results

Table 1 compares the tensile strengths of concrete as determined from three different loading directions. The anisotropic tensile strengths of concrete are nearly similar due to homogeneity of bonding between concrete materials as well as random accumulation of weak plane in concrete mortar.

3.4.1. Numerical modelling of pre-holed specimens by a higher order displacement discontinuity method

In this research, the displacement discontinuities along the boundary can be achieved more accurately by using higher order displacement discontinuity (DD) elements (e.g. quadratic or cubic DD elements). These elements are important for the numerical analyses of pre-holed discs, rectangular concrete specimens, and their breaking mechanism.

In the higher order displacement discontinuity modelling of pre-holed rock-like specimens, the cubic (third order) variation of displacement discontinuity (DD) is assumed along each boundary element. A cubic DD element ($D_k(\varepsilon)$) is divided into four equal sub-elements, such that each sub-element contains a central node for which the nodal DD is evaluated
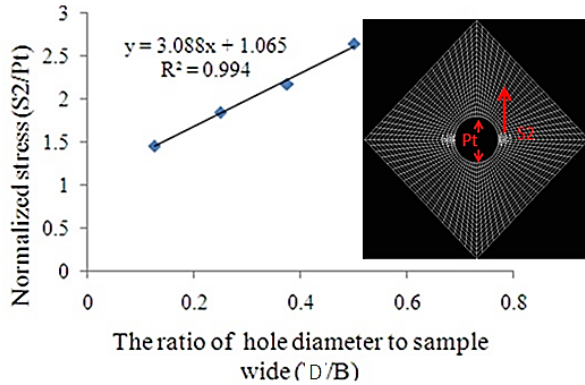
Fig. 8 the variation of normalized tensile stress consecration (S2/Pt) to the ratio of circle diameter to sample wide (D/B).

numerically. The opening displacement discontinuity D_y and the sliding displacement discontinuity D_x can be formulated as:

$$D_k(\varepsilon) = \sum_{i=1}^{4} \Pi_i(\varepsilon) D_k^i, \quad k = x, y$$

Where $D_k^1 (i.e. D_x^1 and D_y^1)$, $D_k^2 (i.e. D_x^2 and D_y^2)$,

$D_k^3 (i.e. D_x^3 and D_y^3)$, and $D_k^4 (i.e. D_x^4 and D_y^4)$ (3)

are the cubic nodal displacement discontinuities and,

$$\Pi_1(\varepsilon) = -\left(3a_1^3 - a_1^2\varepsilon - 3a_1\varepsilon^2 + \varepsilon^3\right)/\left(48a_1^3\right),$$
$$\Pi_2(\varepsilon) = \left(9a_1^3 - 9a_1^2\varepsilon - a_1\varepsilon^2 - \varepsilon^3\right)/\left(16a_1^3\right),$$
$$\Pi_3(\varepsilon) = \left(9a_1^3 + 9a_1^2\varepsilon - a_1\varepsilon^2 - \varepsilon^3\right)/\left(16a_1^3\right),$$
$$\Pi_4(\varepsilon) = -\left(3a_1^3 + a_1^2\varepsilon - 3a_1\varepsilon^2 - \varepsilon^3\right)/\left(48a_1^3\right)$$
(4)

are the cubic collocation shape functions, using $a_1 = a_2 = a_3 = a_4$. A cubic element has four nodes, which are the centres of its four sub-elements as shown in Figure 9.

The potential functions f(x,y), and g(x,y) for the cubic case can be determined from:

$$f(x,y) = \frac{-1}{4\pi(1-\nu)} \sum_{i=1}^{4} D_x^i F_i(I_0, I_1, I_2)$$

$$g(x,y) = \frac{-1}{4\pi(1-\nu)} \sum_{i=1}^{4} D_y^i F_i(I_0, I_1, I_2)$$
(5)

in which, the common function F_i, is defined as

$$F_i(I_0, I_1, I_2, I_3) = \int \Pi_i(\varepsilon) \ln\left[(x-\varepsilon) + y^2\right]^{\frac{1}{2}} d\varepsilon, \quad i = 1, \text{to } 4$$
(6)

where the integrals I_0, I_1, I_2 and I_3 are expressed as follows:

$$I_0(x,y) = \int \ln\left[(x-\varepsilon)^2 + y^2\right]^{\frac{1}{2}} d\varepsilon,$$

$$I_1(x,y) = \int_{-a}^{a} \varepsilon \ln\left[(x-\varepsilon)^2 + y^2\right]^{\frac{1}{2}} d\varepsilon,$$

(7)

$$I_2(x,y) = \int_{-a}^{a} \varepsilon^2 \ln\left[(x-\varepsilon)^2 + y^2\right]^{\frac{1}{2}} d\varepsilon,$$

$$I_3(x,y) = \int_{-a}^{a} \varepsilon^3 \ln\left[(x-\varepsilon)^2 + y^2\right]^{\frac{1}{2}} d\varepsilon$$

Since the singularities of the stresses and displacements near the holes may reduce their accuracies, special crack tip elements are used to increase the accuracy of the DDs near the crack tips. As shown in Fig. 10, the DD variation for three nodes can be formulated using a special crack tip element containing three nodes (or having three special crack tip sub-elements).

(2)
$$D_k(\varepsilon) = [\Gamma_{C1}(\varepsilon)] D_k^1(a) + [\Gamma_{C2}(\varepsilon)] D_k^2(a) + [\Gamma_{C3}(\varepsilon)] D_k^3(a), \quad k = x, y$$
(8)

where the crack tip element has a length $a_1 = a_2 = a_3$. Therefore, considering a crack tip element with three equal sub-elements ($a_1 = a_2 = a_3$), the shape functions, $\Gamma_{C1}(\varepsilon)$, $\Gamma_{C2}(\varepsilon)$ and $\Gamma_{C3}(\varepsilon)$ can be obtained as

$$\Gamma_{C1}(\varepsilon) = \frac{15\varepsilon^{\frac{1}{2}}}{8a_1^{\frac{1}{2}}} - \frac{\varepsilon^{\frac{3}{2}}}{a_1^{\frac{3}{2}}} + \frac{\varepsilon^{\frac{5}{2}}}{8a_1^{\frac{5}{2}}},$$

$$\Gamma_{C2}(\varepsilon) = \frac{-5\varepsilon^{\frac{1}{2}}}{8a_1^{\frac{1}{2}}} + \frac{3\varepsilon^{\frac{3}{2}}}{2\sqrt{3}a_1^{\frac{3}{2}}} - \frac{\varepsilon^{\frac{5}{2}}}{4\sqrt{3}a_1^{\frac{5}{2}}},$$
(9)

$$\Gamma_{C3}(\varepsilon) = \frac{3\varepsilon^{\frac{1}{2}}}{8\sqrt{5}a_1^{\frac{1}{2}}} - \frac{\varepsilon^{\frac{3}{2}}}{2\sqrt{5}a_1^{\frac{3}{2}}} + \frac{\delta^{\frac{5}{2}}}{8\sqrt{5}a_1^{\frac{5}{2}}}$$

$$F_C(x,y) = \frac{-1}{4\pi(1-\nu)} \int_{-a}^{a} D_k(\varepsilon) \ln\left[(x-\varepsilon)^2 + y^2\right]^{\frac{1}{2}} d\varepsilon$$
(10)

Inserting the common displacement discontinuity function, $D_k(\varepsilon)$ (equation (8) in equation (10)) gives:

$$F_C(x,y) = \frac{-1}{4\pi(1-\nu)} \{[\int_{-a}^{a} \Gamma_{C1}(\varepsilon) \ln\left[(x-\varepsilon)^2 + y^2\right]^{\frac{1}{2}} d\varepsilon] D_k^1 +$$

$$[\int_{-a}^{a} \Gamma_{C2}(\varepsilon) \ln\left[(x-\varepsilon)^2 + y^2\right]^{\frac{1}{2}} d\varepsilon] D_k^2 + [\int_{-a}^{a} \Gamma_{C3}(\varepsilon) \ln\left[(x-\varepsilon)^2 + y^2\right]^{\frac{1}{2}} d\varepsilon] D_k^3 \}$$
(11)

Inserting the shape functions, $\Gamma_{C1}(\varepsilon)$, $\Gamma_{C2}(\varepsilon)$ and $\Gamma_{C3}(\varepsilon)$ in equation (11) after some manipulations and rearrangements, the following three special integrals are deduced:

Table 1. Results of direct tensile strength in three different directions.

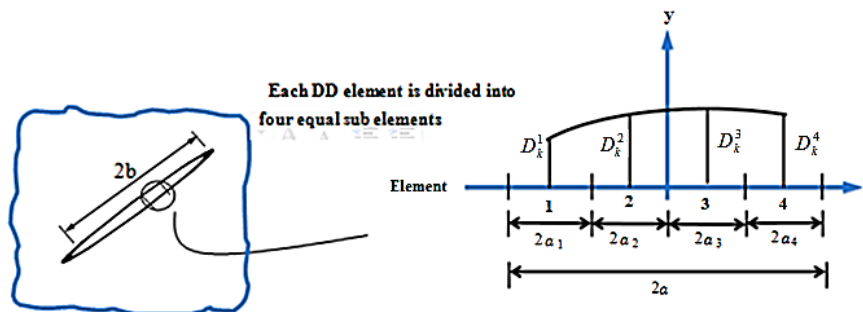| Sample No. (W/B=0. 5)	Tensile strength (MPa) when vertical sides of sample are parallel to the loading axis	Tensile strength (MPa) when vertical sides of sample are returned 45° non counter clock wise related to the loading direction	Tensile strength (MPa) when vertical sides of sample are returned 45° counter clock wise related to the loading direction
1	3.1	3.16	3.19
2	3.08	3.2	3.21
Average	3.09	3.18	3.2

Fig. 9. Cubic shape function showing the variation of higher order displacement discontinuities along an ordinary boundary element

$$I_{C1}(x,y) = \int_{-a}^{a} \varepsilon^{\frac{1}{2}} \ln\left[(x-\varepsilon)^2 + y^2\right]^{\frac{1}{2}} d\varepsilon,$$

$$I_{C2}(x,y) = \int_{-a}^{a} \varepsilon^{\frac{3}{2}} \ln\left[(x-\varepsilon)^2 + y^2\right]^{\frac{1}{2}} d\varepsilon \qquad (12)$$

$$I_{C3}(x,y) = \int_{-a}^{a} \varepsilon^{\frac{5}{2}} \ln\left[(x-\varepsilon)^2 + y^2\right]^{\frac{1}{2}} d\varepsilon$$

Based on linear elastic fracture mechanics (LEFM) principles, the Mode I and Mode II stress intensity factors, K_I and K_{II}, (expressed in MPa m$^{1/2}$), can be written in terms of normal and shear displacement discontinuities obtained for the last special crack tip element near the hole, as follows [47–53]:

$$K_I = \frac{\mu}{4(1-\nu)}\left(\frac{2\pi}{a_1}\right)^{\frac{1}{2}} D_y(a_1), \quad \text{and} \quad K_{II} = \frac{\mu}{4(1-\nu)}\left(\frac{2\pi}{a_1}\right)^{\frac{1}{2}} D_x(a_1)$$

$$(13)$$

Where μ is the shear modulus and ν is Poisson's ratio of the brittle material.

3.4.2. Numerical analysis

The cubic element formulation of two dimensional displacement discontinuities, along with three special crack tip elements, are used to develop a computer program for the solution of plane elasticity crack problems. This method uses four collocation points for each boundary element (i.e. two sub-elements on either side of the centre of the element in question), and is modified to model electrostatic and crack problems in finite, infinite, and semi-infinite planes. A third order (cubic) distribution of displacement discontinuities is assumed along each boundary element with only two degrees of freedom. This approach is more efficient and improves the accuracy of the conventional displacement discontinuity method. Although using three special elements for the treatment of each crack tip is somewhat complicated, it greatly increases the accuracy of displacement discontinuity variations near these singular ends.
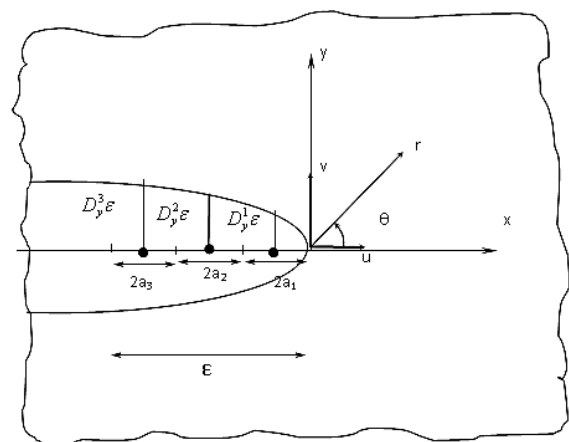

Fig. 10. Special crack tip element with four equal sub-elements

The Linear Elastic Fracture Mechanics (LEFM) concept is used to compute Mode I and Mode II stress intensity factors (SIFs). The σ-criterion is also implemented in the computer code to predict the possibility of crack propagation and estimate the crack initiation direction.

The crack propagation paths are estimated by an incremental crack extension (of length Δb=0.1b) in the predicted direction, by using a standard iterative. In the present analysis, to investigate the crack propagation and cracks coalescence phenomenon, single holes with different diameters, as well as multiple small holes in disc and rectangular specimens, are considered at the centre of a disc specimen and loaded diametrically (under compression). The propagation paths of the emanating cracks from each hole are estimated by the iterative method, and the coalescence of the cracks and holes in specimens containing multiple holes is observed. In this iterative method, the cubic displacement discontinuity elements (i.e. using relatively smaller number of elements but larger

number of nodes) give accurate results for Mode I and Mode II stress intensity factors.

3.4.3. Cracking boundaries for rectangular specimens

In the simulation of the rectangular specimens, the discretization of the cracking boundaries have been accomplished by using 20 cubic elements along rectangular specimens and 10 cubic elements along each internal ring (Fig.11). In addition, the crack propagation angle θ for each crack has been calculated in different steps, by incrementally extending the crack length in the direction of θ for about *1-2* mm in each step. Two cubic elements are taken along each crack increment and three crack tip elements are also added to the last crack increment. In the numerical modelling, the ratio of crack tip length, *L,* to the crack length, *b,* is *0.2* (*L/b =0.2*). Three special crack tip elements are used.

Fig 12 shows the crack growth in numerical models. As can be seen, two tensile cracks begin from both sides of the hole and propagate horizontally till restricted in the middle of the model.
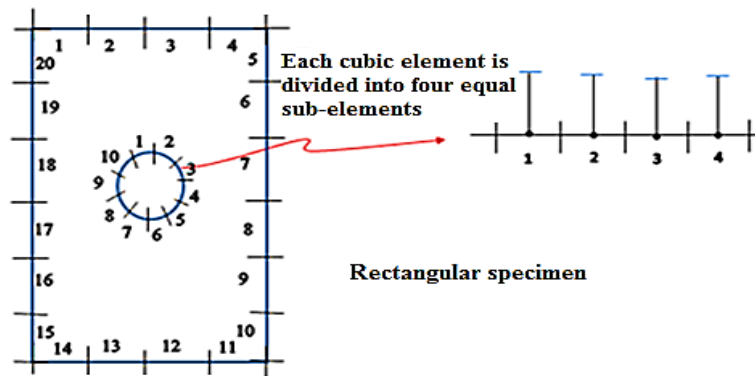

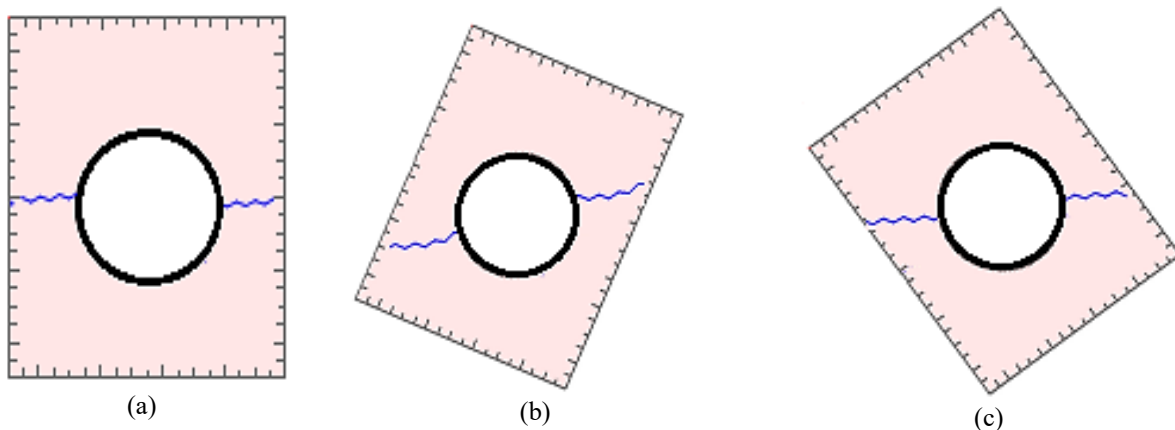Fig.11 discretization of the cracking boundaries for rectangular specimen

(a)   (b)   (c)

Fig. 12. Numerical simulation of the crack propagation paths and cracks coalescence for rectangular specimens

4. Discussions and Conclusions

The CTT device is designed to obtain the anisotropic tensile strengths of concrete under uniaxial tension, and to induce extension failure under true uniaxial tensile stress. The pore diameter at the mid-section of the specimen is 75mm, which may raise an issue regarding the impact of circle size on the measured strengths. The effect of the circle size on concrete tensile strength has been determined using numerical simulation. It has been concluded that as the circle size increases, the tensile stress concentration at the corners increases in terms of constant far-field stress. The real concrete tensile strength is calculated based on Eq. 1. It is understood here that the anisotropic tensile strength of concrete is nearly similar due to homogeneity of bonding between concrete materials, and also due to random accumulation of weak plane in concrete mortar. Fracnc2d simulation and DDM simulation show that there is good accordance between the numerical model and experimental results.

Refrences

BS1881-117 (1983) Testing Concrete - Method for determination of tensile splitting strength. British Standards Institute, London.

Calixto JMF (2002) Experimental investigation of tensile behavior of high strength concrete, *Materials Research* 5 (3):295-303.

De Larrard F, Malier Y (1992) Engineering properties of very high performance concrete, *High Performance Concrete: From Material to Structure*:85-114.

Gerges NN, Issa CA, Fawaz S (2015) Effect of construction joints on the splitting tensile strength of concrete, *Case Studies in Construction Materials* 3:83-91.

Gomez J, Shukla A, Sharma A (2001) Static and dynamic behavior of concrete and granite in tension with damage, *Theoretical and Applied Fracture Mechanics* 36:37-49.

Ibrahim MW, Hamzah A, Jamaluddin N, Ramadhansyah P, Fadzil A (2015) Split Tensile Strength on Self-compacting Concrete Containing Coal Bottom Ash, *Procedia-Social and Behavioral Sciences* 195:2280-2289.

Liu X, Nie Z, Wu S, Wang C (2015) Self-monitoring application of conductive asphalt concrete under indirect tensile deformation, *Case Studies in Construction Materials* 3:70-77.

Mobasher B, Bakhshi M, Barsby C (2014) Backcalculation of residual tensile strength of regular and high performance fiber reinforced concrete from flexural tests, *Construction and Building Materials* 70:243-253.

Silva R, De Brito J, Dhir R (2015) Tensile strength behaviour of recycled aggregate concrete, *Construction and Building Materials* 83:108-118.

Swaddiwudhipong S, Lu H-R, Wee T-H (2003) Direct tension test and tensile strain capacity of concrete at early age, *Cement and Concrete Research* 33:2077-2084.

Wawrzynek PA, Ingraffea A (1987) Interactive finite element analysis of fracture processes: an integrated approach, *Theoretical and Applied Fracture Mechanics* 8:137-150.

Zain MFM, Mahmud H, Ilham A, Faizal M (2002) Prediction of splitting tensile strength of high-performance concrete, *Cement and Concrete Research* 32:1251-1258.

Zheng W, Kwan A, Lee P (2001) Direct tension test of concrete, *Materials Journal* 98:63-71.

Zhou FP (1988) Some aspects of tensile fracture behaviour and structural response of cementitious materials, *Report TVBM 1008.*